Journal of Physics: Condensed Matter

PAPER • **OPEN ACCESS**

LO-mode phonon of KCl and NaCl at 300 K by inelastic x-ray scattering measurements and first principles calculations

To cite this article: Atsushi Togo *et al* 2022 *J. Phys.: Condens. Matter* **34** 365401

View the article online for updates and enhancements.

You may also like

- Elastic properties of type-I clathrate $K_8Zn_4Sn_{42}$ determined by inelastic X-ray scattering
Bogdan M. Leu, Mihai I. Sturza, Jiawang Hong et al.

- Lattice dynamics in the paraelectric phase of $PbHfO_3$ studied by inelastic x-ray scattering
R G Burkovsky, D Andronikova, Yu Bronwald et al.

- Pressure dependence of transverse acoustic phonon energy in ferropericlase across the spin transition
Hiroshi Fukui, Alfred Q R Baron, Daisuke Ishikawa et al.

This content was downloaded from IP address 144.213.253.16 on 27/01/2023 at 08:18

OPEN ACCESS
IOP Publishing
Journal of Physics: Condensed Matter
J. Phys.: Condens. Matter **34** (2022) 365401 (14pp)
https://doi.org/10.1088/1361-648X/ac7b01

LO-mode phonon of KCl and NaCl at 300 K by inelastic x-ray scattering measurements and first principles calculations

Atsushi Togo[1,2,*], **Hiroyuki Hayashi**[3], **Terumasa Tadano**[4], **Satoshi Tsutsui**[5,6] **and Isao Tanaka**[2,3,7]

[1] Research and Services Division of Materials Data and Integrated System, National Institute for Materials Science, Tsukuba, Ibaraki 305-0047, Japan
[2] Center for Elements Strategy Initiative for Structural Materials, Kyoto University, Sakyo, Kyoto 606-8501, Japan
[3] Department of Materials Science and Engineering, Kyoto University, Sakyo, Kyoto 606-8501, Japan
[4] Research Center for Magnetic and Spintronic Materials, National Institute for Materials Science, Tsukuba, Ibaraki 305-0047, Japan
[5] Japan Synchrotron Radiation Research Institute, Sayo-cho, Hyogo 679-5198, Japan
[6] Institute of Quantum Beam Science, Graduate School of Science and Engineering, Ibaraki University, Hitachi, Ibaraki 316-8511, Japan
[7] Nanostructures Research Laboratory, Japan Fine Ceramics Center, Atsuta, Nagoya 456-8587, Japan

E-mail: togo.atsushi@gmail.com

Received 22 April 2022, revised 6 June 2022
Accepted for publication 21 June 2022
Published 1 July 2022

Abstract

Longitudinal-optical (LO) mode phonon branches of KCl and NaCl were measured using inelastic x-ray scattering (IXS) at 300 K and calculated by the first-principles phonon calculation with the stochastic self-consistent harmonic approximation. Spectral shapes of the IXS measurements and calculated spectral functions agreed well. We analyzed the calculated spectral functions that provide higher resolutions of the spectra than the IXS measurements. Due to strong anharmonicity, the spectral functions of these phonon branches have several peaks and the LO modes along Γ–L paths are disconnected.

Keywords: KCl, NaCl, inelastic x-ray scattering, phonon calculation, anharmonicity

(Some figures may appear in colour only in the online journal)

* Author to whom any correspondence should be addressed.

Original Content from this work may be used under the terms of the Creative Commons Attribution 4.0 licence. Any further distribution of this work must maintain attribution to the author(s) and the title of the work, journal citation and DOI.

 © 2022 The Author(s). Published by IOP Publishing Ltd

1. Introduction

Phonons are the quanta related to collective vibrations of atoms in crystal, and known to play important roles in determining a variety of crystal properties such as heat capacity, thermal expansion, and thermal conductivity. Phonons in Brillouin zones of crystals have been measured using inelastic neutron and x-ray scatterings, and we can find phonon band structures of those crystals in literature. In the last decades, computational advances to solve electronic Schrödinger equation within the density functional theory [1, 2] (DFT) enabled us to predict phonon properties [3–7]. Due to its strong predictability, nowadays, phonon calculation is applied to studies in various scientific fields as an essential tool.

The formulation of phonons involves a transformation from describing the potential in terms of the individual atomic displacements to normal modes, which describe collective displacements [8, 9]. In many crystals at modest temperatures, phonon properties of crystals are often well reproduced in perturbation theory, where Taylor expansion of crystal potential with respect to atomic displacements is truncated at lowest order terms as a good approximation. As a result, the computational procedure of the phonon calculation becomes simple and the practical application is made systematic. This is one of the reasons that the phonon calculation has become popular in scientific research. The majority of reported phonon calculations are limited to the harmonic approximation since it often provides satisfactory accuracy for the research purposes, and, in practice it is much less computationally demanding than a beyond-harmonic treatment.

Crystals for which it is difficult to apply straightforward perturbation theory may be categorized as anharmonic crystals. Anharmonicity is a ubiquitous phenomenon, that is related to properties of materials such as thermal expansion, lattice thermal conductivity, and structural phase transition [9, 10]. When we study anharmonic crystals, it is important to know the phonon spectral shapes, for which the harmonic approximation is insufficient. Recent progress of computational methodologies in anharmonic phonon calculations [11–14] has enabled us to simulate phonon spectra of anharmonic crystals. Many researches on anhamonicity have been achieved by combining experimental and calculation methods [15–21]. However, comparison of detailed phonon spectral shapes between experiments and calculations is nontrivial since high-resolution experimental measurements are limited.

The purpose of this work is to verify an anharmonic phonon calculation method employed in this study by experiments and to establish the systematic computational procedure. Inelastic neutron scattering (INS) [18, 22] and inelastic x-ray scattering (IXS) [17, 19] have been employed to investigate anharmonic phonons at finite wave vectors as complementary techniques [20, 21]. In the former technique, the relation between momentum and energy transfer is represented as [10, 23]

$$\Delta E = \frac{\hbar^2}{2m_{\mathrm{n}}}\left(2\mathbf{k}_{\mathrm{f}} - \mathbf{Q}\right)\cdot\mathbf{Q}, \tag{1}$$

where $\hbar$, ΔE, $\mathbf{Q}$, $\mathbf{k}_{\mathrm{f}}$, and m_{n} represent the reduced Planck constant, the energy transfer, the momentum transfer, the momentum of neutron after scattering, and the mass of a neutron, respectively. This demonstrates that the momentum transfer is always coupled with the energy transfer. This also means that the energy resolution depends on both momentum and energy transfers. In the latter case, on the other hand, the energy transfer is nearly independent of the momentum transfer, which means that the energy resolution is also approximately independent from momentum and energy transfers [24]. In addition, intensity of background noise is nearly ignored in IXS spectra. Therefore, IXS experiments were simpler and more preferable to INS experiments for us to perform the comparison of detailed anharmonic phonon spectra between experiments and calculations in wide $\mathbf{Q}$-ω space.

Phonon measurements using INS were reported for KCl [25] and NaCl [26, 27] at 300 K (room temperature). Phonon frequencies measured in these studies are plotted in figures 1 and 2, for which the phonon frequency values in figure 2 of [27] were sampled using WebPlotDigitizer [28]. Recently, detailed calculation of phonon band structure of NaCl was reported by Ravichandran and Broido [29]. They employed a phonon renormalization approach to treat strong anharmonicity in NaCl, and showed good agreement of the phonon frequencies with the measurement by Raunio *et al* [26].

In this study, we investigate phonon spectral shapes of the longitudinal-optical (LO) modes of KCl and NaCl using the IXS measurements and first-principles anharmonic phonon calculations. In particular, their LO-mode phonons near Γ-points are shown to be strongly anharmonic. In sections 2 and 3, methods of measurements and calculations are described, respectively. In section 4, first we discuss about feasibility of the calculation results against the IXS measurements by the peak positions and shapes of the phonon spectra, then we analyze the calculated spectral functions in details.

2. Experimental method

The phonon spectra were measured using IXS at the BL35XU of the SPring-8 synchrotron [30–33]. The energy of 21.747 keV of the beam and Si $\begin{pmatrix}11 & 11 & 11\end{pmatrix}$ backscattering setup with energy resolution of ∼1.5 meV were used.

The phonon spectra of KCl and NaCl were measured around the Γ–L path of $\mathbf{Q} = (3-u\ \ 3-u\ \ 3-u)$ and $\mathbf{Q} = (3+u\ \ 3+u\ \ 3+u)$ with positive u, respectively, where the points in the reciprocal spaces are represented with respect to the reciprocal basis vectors of the conventional unit cell. Their Q-resolutions were $\Delta\mathbf{Q} \sim \begin{pmatrix}0.03 & 0.02 & 0.04\end{pmatrix}$ and $\Delta\mathbf{Q} \sim \begin{pmatrix}0.03 & 0.03 & 0.01\end{pmatrix}$, respectively. For KCl, those along the Γ–X path of $\mathbf{Q} = \begin{pmatrix}5-u & 1 & 1\end{pmatrix}$ were also measured, and the Q-resolution was $\Delta\mathbf{Q} \sim \begin{pmatrix}0.04 & 0.00 & 0.04\end{pmatrix}$. Due to the experimental setting, measured Q-points slightly deviated from the high-symmetry paths for efficient use of the analyzer array [31–33] and the coordinates are shown in figures 3–5 along with the measured spectra. Lorentzian functions were used to determine the peak positions of the

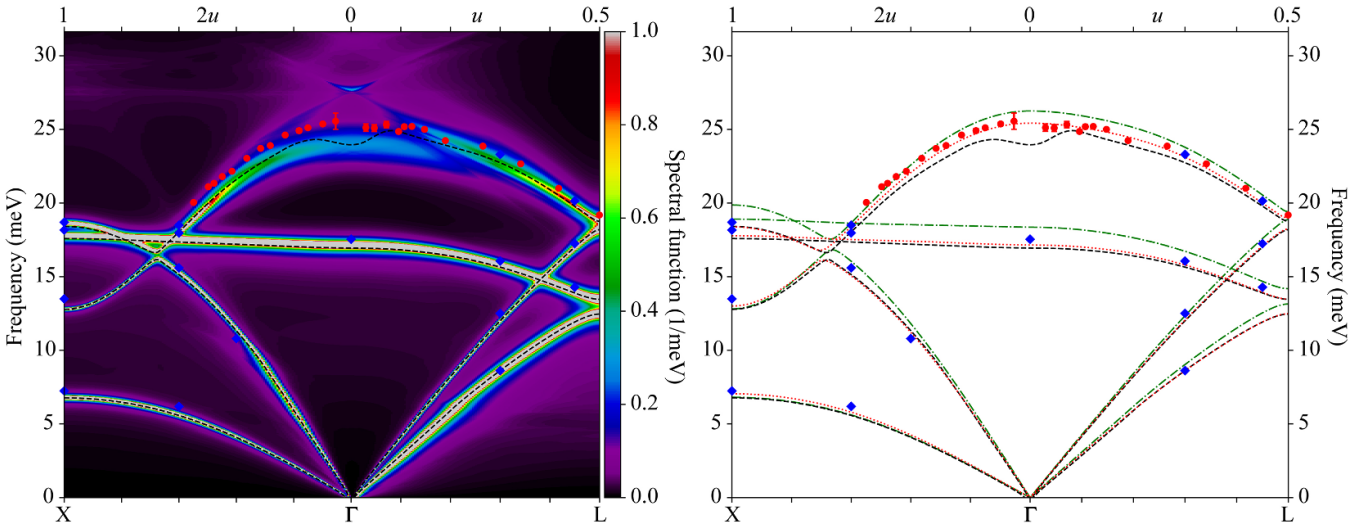

Figure 1. (Left panel) Phonon spectral function of KCl, $\sum_\nu A_{\mathbf{q}\nu}(\omega)$, along X–Γ–L path at 300 K. (Right panel) Phonon band structure of KCl along X–Γ–L path at 300 K. The (green) dashed-dotted curves show the renormalized frequencies ($\Omega_{\mathbf{q}\nu}$), the (black) dashed curves depict the renormalized frequencies shifted by the real part of the self-energy ($\Delta_{\mathbf{q}\nu}(\Omega_{\mathbf{q}\nu})$) and the (red) dotted curves show the harmonic frequencies. The filled circle and diamond symbols show peak positions of the IXS spectra by our measurement and the INS measurement by Raunio and Almqvist [25], respectively.

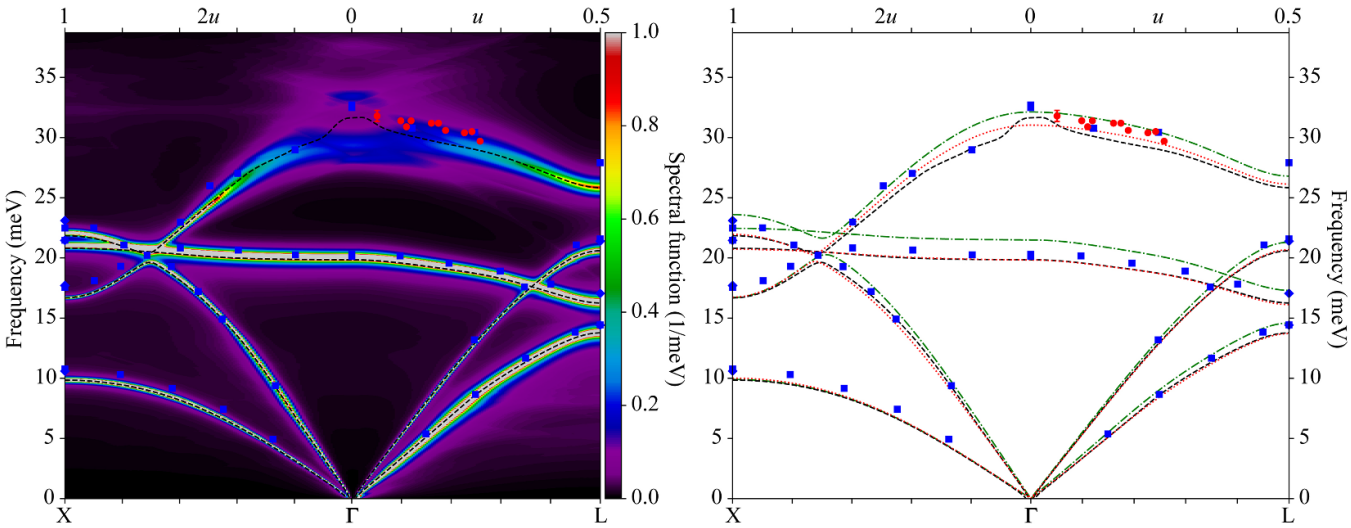

Figure 2. (Left panel) Phonon spectral function of NaCl, $\sum_\nu A_{\mathbf{q}\nu}(\omega)$, along X–Γ–L path at 300 K. (Right panel) Phonon band structure of NaCl along X–Γ–L path at 300 K. The (green) dashed-dotted curves show the renormalized frequencies, ($\Omega_{\mathbf{q}\nu}$), the (black) dashed curves depict the renormalized frequencies shifted by the real part of the self-energy, ($\Delta_{\mathbf{q}\nu}(\Omega_{\mathbf{q}\nu})$), and the (red) dotted curves show the harmonic frequencies. The filled circle symbols show peak positions of the IXS spectra by our measurement. The filled diamond and square symbols depict the INS measurements by Raunio *et al* [26] and by Schmunk and Winder [27], respectively.

phonon spectra by least-squares fitting, and the determined points are presented in figures 1 and 2.

3. Method of calculation

3.1. Phonon spectral function

Anharmonic phonon calculations were performed in the stochastic self-consistent harmonic approximation (SSCHA) [12, 34–40]. There exist several software implementations of SSCHA. The SSCHA code [40] is the software implementation of the original SSCHA method. The hiPhive code [41] has an implementation of a self-consistent harmonic approximation (SCHA) resembling [34]. We employed an iterative force-constants-fitting approach within the framework of SSCHA which is considered equivalent to the methods reported in [42, 43] as implemented in the QSCAILD code [42] and the TDEP code [44–46], respectively.

SCHA force constants are given as

$$\Phi_{l\kappa j,l'\kappa' j'} = \left\langle \frac{\partial^2 V}{\partial u_{l\kappa j}\partial u_{l'\kappa' j'}} \right\rangle_{\tilde{\rho}_\Phi}, \tag{2}$$

where V is the crystal potential and $u_{l\kappa j}$ is the atomic displacement at the lattice point l, atom κ of l, and Cartesian index j.

The angle bracket means average with respect to the density matrix of harmonic phonons $\tilde{\rho}_\Phi$, where $\tilde{\rho}_\Phi$ is a function of Φ at a temperature T, i.e. equation (2) is a self-consistent equation at T. Displacements of atoms in direct space are represented by superposition of phonon normal modes with amplitudes $Q_{\mathbf{q}\nu}$, where $\mathbf{q}$ and ν are the wave vector and the band index, respectively. The probability distribution function of each harmonic phonon mode $(\mathbf{q},\nu)$ at T, $P_{\mathbf{q}\nu}(T)$, is given as [23, 47]

$$P_{\mathbf{q}\nu}(T) = \frac{1}{\sqrt{2\pi\sigma^2_{\mathbf{q}\nu}(T)}} \exp\left[-\frac{1}{2}\frac{Q^2_{\mathbf{q}\nu}}{\sigma^2_{\mathbf{q}\nu}(T)}\right], \tag{3}$$

$$\sigma^2_{\mathbf{q}\nu}(T) = \frac{\hbar}{2\Omega_{\mathbf{q}\nu}}[1+2n_{\mathbf{q}\nu}(T)],\ n_{\mathbf{q}\nu}(T) = \frac{1}{\mathrm{e}^{\hbar\Omega_{\mathbf{q}\nu}/k_\mathrm{B}T}-1},$$

where k_B denotes the Boltzmann constant. $\Omega_{\mathbf{q}\nu}$ is the phonon frequency as the solution of dynamical matrix of Φ in equation (2). The density matrix $\tilde{\rho}_\Phi$ in equation (2) corresponds to the product of $P_{\mathbf{q}\nu}(T)$, i.e. $\prod_{\mathbf{q}\nu} P_{\mathbf{q}\nu}(T)$.

The third-order force constants with respect to $\tilde{\rho}_\Phi$ are given as [36, 38–40]

$$\Phi^{\tilde{\rho}_\Phi}_{l\kappa j, l'\kappa' j', l''\kappa'' j''} = \left\langle \frac{\partial^3 V}{\partial u_{l\kappa j}\partial u_{l'\kappa' j'}\partial u_{l''\kappa'' j''}} \right\rangle_{\tilde{\rho}_\Phi}. \tag{4}$$

With equations (2) and (4), spectral function of each phonon mode [36] was calculated from the following form [48]:

$$A_{\mathbf{q}\nu}(\omega) = \frac{1}{\pi}\frac{4\Omega^2_{\mathbf{q}\nu}\Gamma_{\mathbf{q}\nu}(\omega)}{\left[\omega^2-\Omega^2_{\mathbf{q}\nu}-2\Omega_{\mathbf{q}\nu}\Delta_{\mathbf{q}\nu}(\omega)\right]^2+\left[2\Omega_{\mathbf{q}\nu}\Gamma_{\mathbf{q}\nu}(\omega)\right]^2}, \tag{5}$$

where ω is the phonon frequency sampled arbitrary in the calculation, $\Delta_{\mathbf{q}\nu}(\omega)$ and $\Gamma_{\mathbf{q}\nu}(\omega)$ denote the real and imaginary parts of the self-energy of the bubble diagram, respectively, whose details are written in appendix A.

To compute equations (2) and (4), supercell approach was used. Finite atomic displacements in supercells were generated by stochastically sampling normal mode amplitudes $Q_{\mathbf{q}\nu}$ on the probability distribution functions of $P_{\mathbf{q}\nu}(T)$ at the commensurate q-points. Force constants were obtained from atomic displacements and forces by linear regression [48], where the forces were calculated using first-principles calculation. More computational details are given in the next section.

3.2. Computational details

For the conventional unit cell models, experimental lattice parameters of 6.29 and 5.64 Å at 300 K for KCl and NaCl [49], respectively, were used. For the supercell phonon calculation, we employed the phonopy [50] and phono3py [51] codes. Non-analytical term correction [5, 6, 52] was applied to dynamical matrices to treat long range dipole-dipole interactions. For force constants fitting, the ALM code [48] was used. Supercells of $2\times2\times2$ expansion of conventional unit cells of KCl and NaCl were used for most of the harmonic and anharmonic phonon calculations. In addition, $4\times4\times4$ supercells were used for the calculations of the harmonic force constants to replace harmonic part of the SSCHA force constants calculated with the $2\times2\times2$ supercells, i.e. we approximate Φ of equation (2) by $\Phi_{4\times4\times4} \sim \Phi^{(0)}_{4\times4\times4} + \Phi_{2\times2\times2} - \Phi^{(0)}_{2\times2\times2}$, where $\Phi^{(0)}$ denotes the harmonic force constants and the subscript indicates the supercell size.

For the first-principles calculations, we employed the plane-wave basis projector augmented wave (PAW) method [53] within the framework of DFT as implemented in the VASP code [54–56]. The generalized gradient approximation of Perdew, Burke, and Ernzerhof revised for solids (PBEsol) [57] was used as the exchange correlation potential. For PAW datasets of atoms, 3p electrons for K and 2p electrons for Na were treated as valence. Static dielectric constants and Born effective charges were calculated with primitive cells from density functional perturbation theory (DFPT) as implemented in the VASP code [58, 59]. A plane-wave energy cutoff of 500 eV was employed for the supercell force calculations and 750 eV for the DFPT calculations. Reciprocal spaces were sampled by half-shifted $4\times4\times4$ meshes for the $2\times2\times2$ supercells, half-shifted $2\times2\times2$ meshes for the $4\times4\times4$ supercells, and the Γ-centered $8\times8\times8$ meshes for the primitive cells. For each harmonic force constants calculation, atoms in 20 supercells were randomly displaced in directions with a fixed distance of 0.03 Å from their equilibrium positions. The high-frequency dielectric constants (ϵ_∞) of KCl and NaCl were obtained as 2.365 and 2.546, and the Born effective charges as ±1.129 and ±1.096, respectively.

The SSCHA force constants were obtained by iterating phonon calculations. Initial phonon calculation was performed with small displacements (0.03 Å) in supercells. At every iteration step, 20 supercells with random atomic displacements as a batch were generated as given by equation (3) at 300 K using force constants that were calculated with supercell displacement-force datasets of up to previous 50 batches (1000 supercells). Then, forces of the supercells with the generated displacements were calculated using the VASP code. This process was repeated 100 times, and we took the last force constants as the converged SSCHA force constants. Details about the convergence is summarized in appendix B. For the calculation of equation (4), 4000 supercells with random atomic displacements generated from the SSCHA force constants according to equation (3) were used for the fitting of third-order force constants. Commensurate q-points were sampled for equation (3), which guarantees the generation of real valued displacements in the supercells. To perform systematic calculations presented above, we employed the AiiDA environment [60] with the AiiDA-VASP [61] and AiiDA-phonoxpy [62] plugins. For the calculations of the spectral functions, self-energies, and weighted joint density of states, the q-points were sampled on regular grids of $300\times300\times300$ mesh, and the phonon frequencies were uniformly sampled at 2001 points from 0 meV to about twice the highest renormalied phonon frequencies.

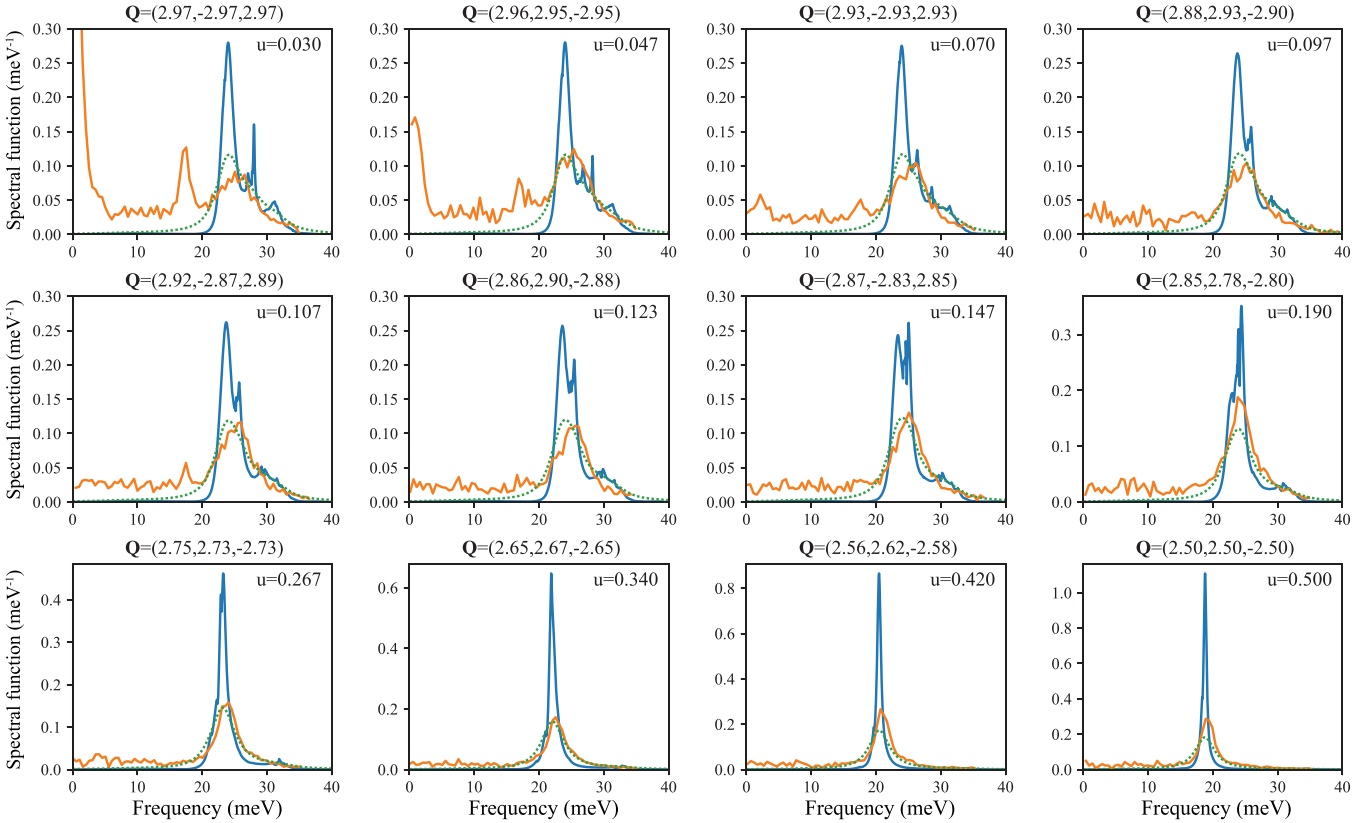

Figure 3. KCl spectra measured by IXS at Q-points (see figure 1) and calculated phonon spectral functions of the LO mode at q-points near the Γ–L path. The (orange) solid curves with broader peaks are the IXS measurements. The (blue) solid and (green) dotted curves show the calculated spectral functions ($A_{\mathbf{q},\mathrm{LO}}(\omega)$) and those smeared by the Lorentzian function with the 1.5 meV scale parameter, respectively. The q-points of the calculation were chosen from the grid points on the Γ–L path at which their distances from the Γ-point are closest to those of the measured Q-points. The q-point is represented by $\mathbf{q} = (u, u, u)$ with respect to the conventional basis of the Bilbao crystallographic server [63], where $u = 0.5$ gives the L-point.

4. Results and discussions

4.1. Phonon band structures

Phonon structures of KCl and NaCl are presented in figures 1 and 2, respectively. The left panels show the calculated spectral functions. The points and curves in the right panels depict experimentally measured and calculated results, respectively. The LO-mode frequencies that we measured agree well with the INS measurements reported in [25–27] for KCl and NaCl.

The calculated spectral functions of the LO modes near the Γ-points show side bands due to their strong anharmonicity. Except for the LO modes, the spectra show clear peaks. We can see the peak positions underestimate the experiments systematically. The underestimation is largest for the LO modes near the Γ-points. However we are satisfied with the current level of the agreements between the calculations and experiments since it is expected that this level of the errors hardly affect the shapes of the calculated spectral functions.

The three curves in the right panel in each of figures 1 and 2 show harmonic frequencies, $\Omega^{(0)}_{\mathbf{q}\nu}$, calculated from $\Phi^{(0)}$, renormalized harmonic frequencies, $\Omega_{\mathbf{q}\nu}$, obtained from Φ of equation (2), and $\Omega_{\mathbf{q}\nu}$ shifted by real parts of the self-energies at $\Omega_{\mathbf{q}\nu}$, $\Omega_{\mathbf{q}\nu} + \Delta_{\mathbf{q}\nu}(\Omega_{\mathbf{q}\nu})$. By cancellation between the renormalizations $\Omega_{\mathbf{q}\nu} - \Omega^{(0)}_{\mathbf{q}\nu}$ and the shifts $\Delta_{\mathbf{q}\nu}(\Omega_{\mathbf{q}\nu})$, the harmonic frequencies $\Omega^{(0)}_{\mathbf{q}\nu}$ become close to $\Omega_{\mathbf{q}\nu} + \Delta_{\mathbf{q}\nu}(\Omega_{\mathbf{q}\nu})$ and show even better agreements with the experiments than $\Omega_{\mathbf{q}\nu} + \Delta_{\mathbf{q}\nu}(\Omega_{\mathbf{q}\nu})$ for the LO modes. However, we consider this is a specific result for KCl and NaCl and not general tendency.

As shown in the left panels of figures 1 and 2, for the sharp spectral functions, $\Omega_{\mathbf{q}\nu} + \Delta_{\mathbf{q}\nu}(\Omega_{\mathbf{q}\nu})$ are expected to agree well with their peak positions. Near the Γ-point, since the LO modes exhibit the broad spectral functions, $\Omega_{\mathbf{q},\mathrm{LO}} + \Delta_{\mathbf{q},\mathrm{LO}}(\Omega_{\mathbf{q},\mathrm{LO}})$ are unable to represent their peak positions. This is an effect of the strong anharmonicity.

4.2. Comparisons of spectral shapes

The measured IXS spectra and calculated spectral functions of the LO modes are compared in figures 3–5. The calculated results show the LO-mode contributions only, i.e. what are presented are $A_{\mathbf{q},\mathrm{LO}}(\omega)$. The LO-mode spectra

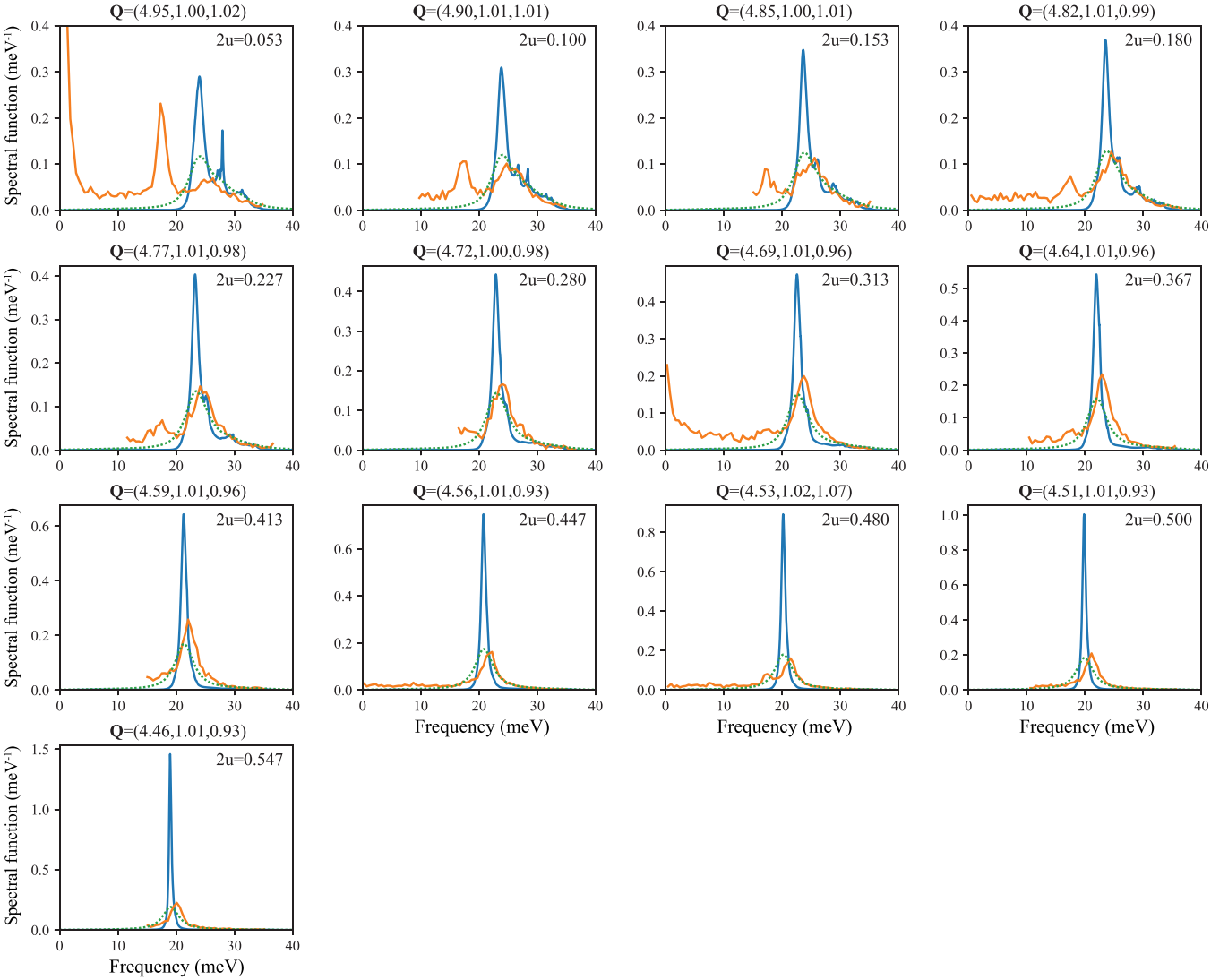

Figure 4. KCl spectra measured by IXS at Q-points (see figure 1) and calculated phonon spectral functions of the LO mode at q-points near the Γ–X path. The (orange) solid curves with broader peaks are the IXS measurements. The (blue) solid and (green) dotted curves show the calculated spectral functions ($A_{\mathbf{q},\mathrm{LO}}(\omega)$) and those smeared by the Lorentzian function with the 1.5 meV scale parameter, respectively. The q-points of the calculation were chosen from the grid points on the Γ–X path at which their distances from the Γ-point are closest to those of the measured Q-points. The q-point is represented by $\mathbf{q} = (2u, 0, 0)$ with respect to the conventional basis of the Bilbao crystallographic server [63], where $2u = 1$ gives the X-point.

show the broader peaks near the Γ-points. With increasing distance from the Γ-points, the spectral peaks become sharper.

The IXS spectra show broader spectral shapes than the calculated spectral functions due to the finite IXS energy resolution. To include this effect in the calculations, the spectral functions were smeared by the Lorentzian function with a scale parameter of the 1.5 meV. The smeared spectral functions are also shown in figures 3–5. We can see that general trend of the IXS spectral shapes are well reproduced by them. Therefore, we consider that details of the anharmonic spectra can be discussed from the calculated spectral functions.

4.3. Spectral functions and self-energies

The spectral function $A_{\mathbf{q}\nu}(\omega)$ in equation (5) is obtained from the renormalized frequency $\Omega_{\mathbf{q}\nu}$ and the real and imaginary parts of the self-energy, $\Delta_{\mathbf{q}\nu}(\omega)$ and $\Gamma_{\mathbf{q}\nu}(\omega)$, respectively. In this section, the spectral functions of the LO modes, $A_{\mathbf{q},\mathrm{LO}}(\omega)$, are analyzed using $\Omega_{\mathbf{q},\mathrm{LO}}$, $\Delta_{\mathbf{q},\mathrm{LO}}(\omega)$, and $\Gamma_{\mathbf{q},\mathrm{LO}}(\omega)$ in detail.

$A_{\mathbf{q},\mathrm{LO}}(\omega)$, $\Delta_{\mathbf{q},\mathrm{LO}}(\omega)$, $\Gamma_{\mathbf{q},\mathrm{LO}}(\omega)$, and $\Omega_{\mathbf{q},\mathrm{LO}}$ at the same q-points used in figures 3–5 are shown in figures 6–8, respectively. As equation (5) indicates, the spectral functions are expected to have strong peaks around $\omega \sim \Omega_{\mathbf{q}\nu} + \Delta_{\mathbf{q}\nu}(\omega)$, which we call main peaks. In these figures, the main peaks are

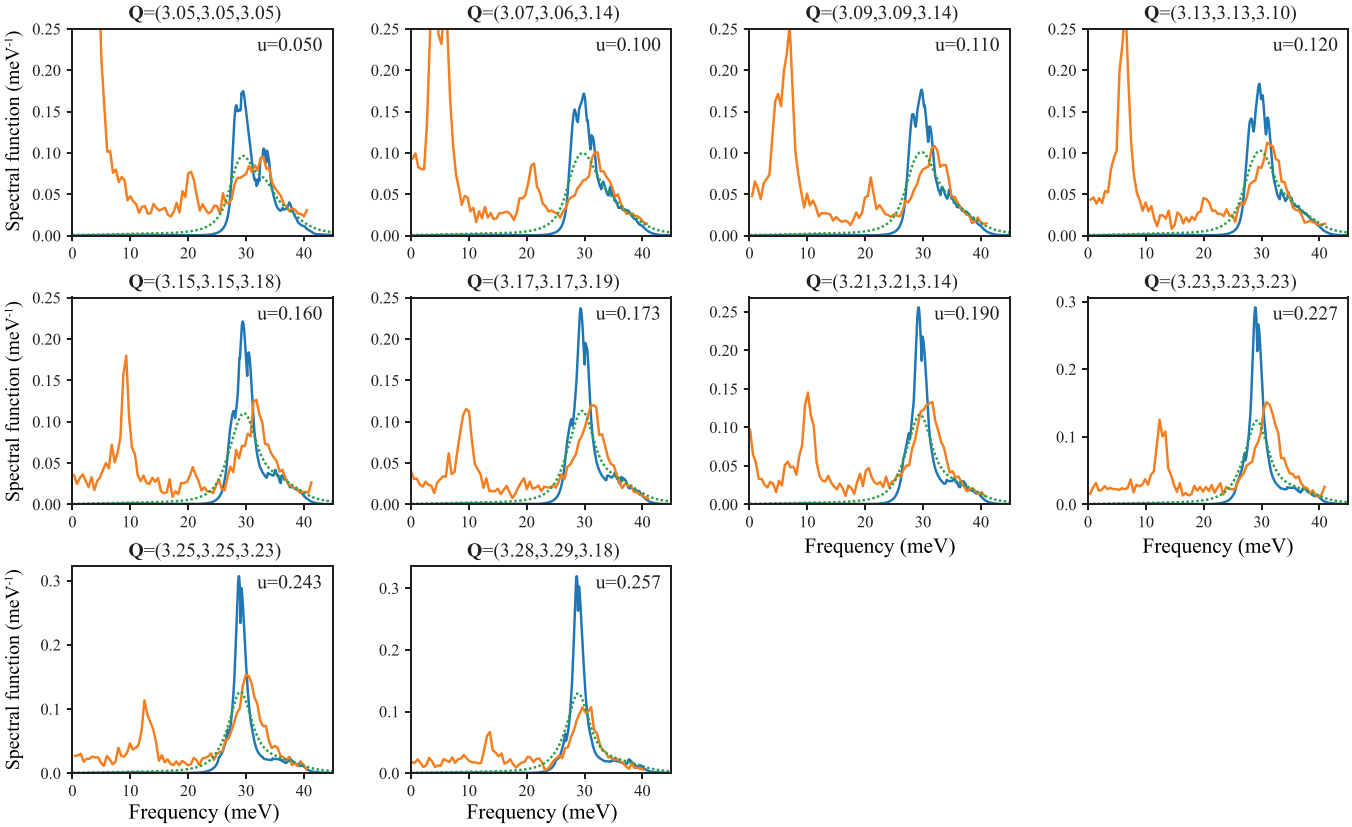

Figure 5. NaCl spectra measured by IXS at Q-points (see figure 2) and calculated phonon spectral functions of the LO mode at q-points near the Γ–L path. The (orange) solid curves with broader peaks are the IXS measurements. The (blue) solid and (green) dotted curves show the calculated spectral functions ($A_{\mathbf{q},\mathrm{LO}}(\omega)$) and those smeared by the Lorentzian function with the 1.5 meV scale parameter, respectively. The q-points of the calculation were chosen from the grid points on the Γ–L path at which their distances from the Γ-point are closest to those of the measured Q-points. The q-point is represented by $\mathbf{q} = (u, u, u)$ with respect to the conventional basis of the Bilbao crystallographic server [63], where $u = 0.5$ gives the L-point.

located a few meV below $\Omega_{\mathbf{q},\mathrm{LO}}$ since $\Delta_{\mathbf{q},\mathrm{LO}}(\omega)$ have negative values near the main peaks.

The spectral functions show other multiple peaks than their main peaks. These peaks become stronger when $\Gamma_{\mathbf{q},\mathrm{LO}}(\omega)$ is larger at ω close to $\Omega_{\mathbf{q},\mathrm{LO}}$. This condition is satisfied at the q-points near the Γ-points. The large $\Gamma_{\mathbf{q},\mathrm{LO}}(\omega)$ is mainly the result of energy and momentum conversations of three phonon scatterings of the class formally denoted as $(\mathbf{q},\omega) \to (\mathbf{q}',\omega_{\nu'}) + (\mathbf{q}'',\omega_{\nu''})$, which is discussed in section 4.4.

The distributions of $\Delta_{\mathbf{q},\mathrm{LO}}(\omega)$ and $\Gamma_{\mathbf{q},\mathrm{LO}}(\omega)$ are presented in figures 9 and 10 similarly to the left panels of figures 1 and 2, respectively, where $\Omega_{\mathbf{q}\nu}$ are superimposed on these figures instead of $\Omega_{\mathbf{q}\nu} + \Delta_{\mathbf{q}\nu}(\Omega_{\mathbf{q}\nu})$. The overall distributions are similar between KCl and NaCl except for their frequency scales. Each of them is roughly symmetric between the Γ–L and Γ–X path sides. In the low frequency domains, the distributions are relatively flat mainly because the term $(n_{\mathbf{q}'\nu'} - n_{\mathbf{q}''\nu''})$ in equation (A4) is well cancelled as discussed in section 4.4. We can see the characteristic distributions in the vicinities of the highest frequencies of $\Omega_{\mathbf{q},\mathrm{LO}}$ near the Γ points, which provides interesting spectral shapes. Large $\Gamma_{\mathbf{q},\mathrm{LO}}(\omega)$ are also found at the high frequency domains near the X-points, however $A_{\mathbf{q},\mathrm{LO}}(\omega)$ are less anharmonic since $\Omega_{\mathbf{q},\mathrm{LO}}$ are low enough to avoid passing through these $(\mathbf{q},\omega)$ domains.

4.4. Three phonon scattering processes

The imaginary part of self-energy $\Gamma_\lambda(\omega)$ in equation (A4) is determined by detailed combinations of $\Phi^{\tilde{\rho}_\Phi}_{\lambda\lambda'\lambda''}$ and energy conservations weighted by phonon occupation numbers. Due to translational symmetry, $\Phi^{\tilde{\rho}_\Phi}_{\lambda\lambda'\lambda''}$ contains momentum conservation as represented by $\Delta(\mathbf{q} + \mathbf{q}' + \mathbf{q}'')$ in equation (A1). Like the previous works [51, 64], in this section, we discuss impacts of the energy and momentum conservations of three phonon scatterings by introducing weighted joint-density-of-states (JDOS). The weighted JDOS $N_2(\mathbf{q},\omega)$ is defined by replacing $\frac{18\,\pi}{\hbar^2}\left|\Phi^{\tilde{\rho}_\Phi}_{-\lambda\lambda'\lambda''}\right|^2$ in equation (A4) by $\frac{1}{N}\Delta(-\mathbf{q} + \mathbf{q}' + \mathbf{q}'')$:

$$N_2(\mathbf{q},\omega) = N_2^{(1)}(\mathbf{q},\omega) + N_2^{(2)}(\mathbf{q},\omega), \tag{6}$$

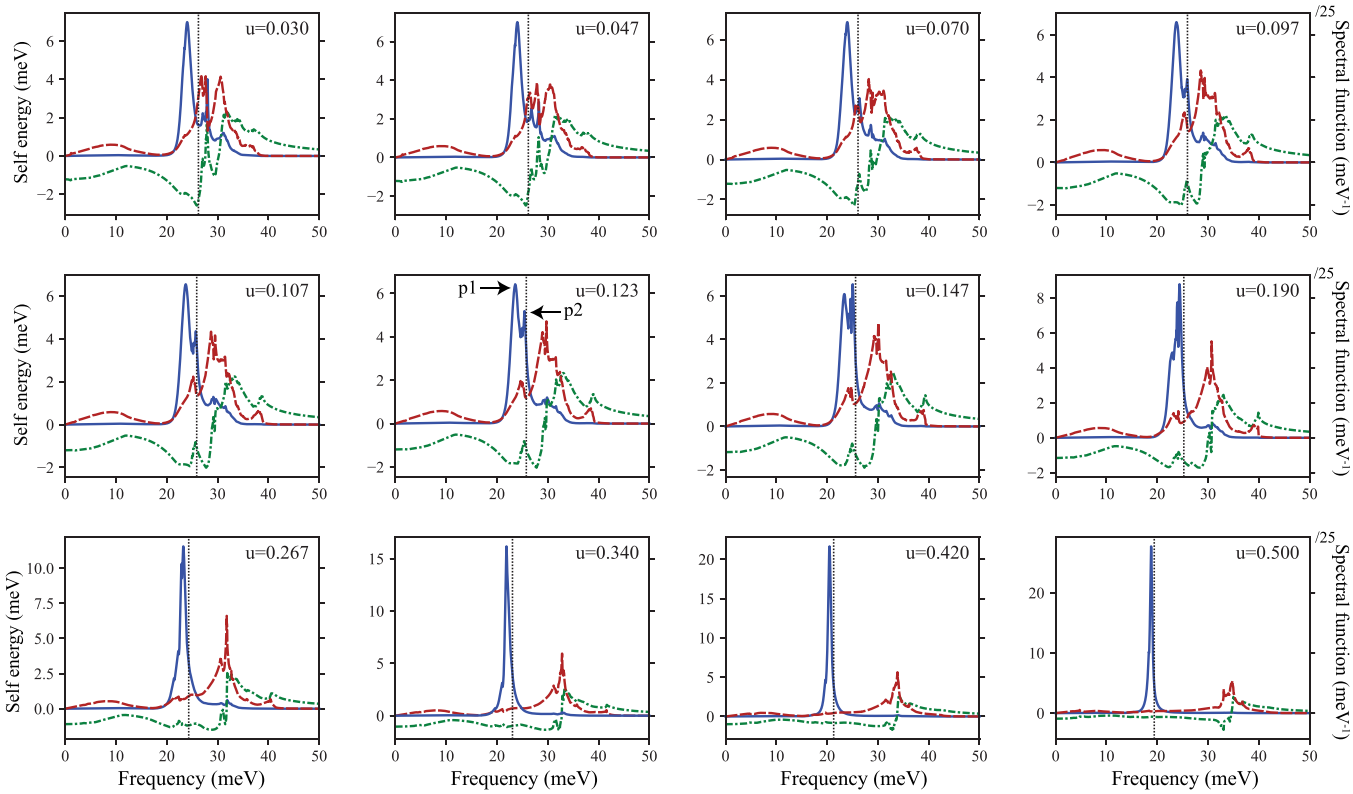

Figure 6. Real and imaginary parts of self-energies and renormalized frequencies of KCl at q-points on the Γ–L path. Each panel corresponds to that in figure 3. The dashed-dotted (green) and dashed (red) curves show the real ($\Delta_{\mathbf{q},\mathrm{LO}}(\omega)$) and imaginary ($\Gamma_{\mathbf{q},\mathrm{LO}}(\omega)$) parts of the self-energies, respectively. The solid (blue) curves show the spectral functions ($A_{\mathbf{q},\mathrm{LO}}(\omega)$), that are the same as those in figure 3. The vertical dotted lines indicate the renormalized frequencies ($\Omega_{\mathbf{q},\mathrm{LO}}$). The small arrows in the panel $u = 0.123$ depict two main peaks that change their intensity ratio at q-points along the Γ–L path.

where

$$N_2^{(1)}(\mathbf{q},\omega) = \frac{1}{N}\sum_{\lambda'\lambda''} \Delta(-\mathbf{q}+\mathbf{q}'+\mathbf{q}'')(n_{\lambda'} - n_{\lambda''}) \times [\delta(\omega + \Omega_{\lambda'} - \Omega_{\lambda''}) - \delta(\omega - \Omega_{\lambda'} + \Omega_{\lambda''})], \tag{7}$$

$$N_2^{(2)}(\mathbf{q},\omega) = \frac{1}{N}\sum_{\lambda'\lambda''} \Delta(-\mathbf{q}+\mathbf{q}'+\mathbf{q}'')(n_{\lambda'} + n_{\lambda''} + 1) \times \delta(\omega - \Omega_{\lambda'} - \Omega_{\lambda''}). \tag{8}$$

Note that the weighted JDOS is independent from the band index. In equation (6), $N_2^{(1)}(\mathbf{q},\omega)$ and $N_2^{(2)}(\mathbf{q},\omega)$ mean the contributions from two different scattering classes as written formally [65],

$$\begin{cases} \text{class 1:} & (\mathbf{q},\omega) + (\mathbf{q}',\Omega_{\lambda'}) \longrightarrow (\mathbf{q}''\Omega_{\lambda''}) \\ \text{class 2:} & (\mathbf{q},\omega) \longrightarrow (\mathbf{q}',\Omega_{\lambda'}) + (\mathbf{q}'',\Omega_{\lambda''}), \end{cases}$$

respectively. $N_2^{(1)}(\mathbf{q},\omega)$ and $N_2^{(2)}(\mathbf{q},\omega)$ of KCl and NaCl at 300 K are shown in figures 11 and 12 in a similar manner to the right panels of figures 9 and 10, respectively. $N_2^{(1)}(\mathbf{q},\omega)$ (left panels) show weaker intensities than $N_2^{(2)}(\mathbf{q},\omega)$ (right panels) due to the term $(n_{\lambda'} - n_{\lambda''})$ in equation (7). $N_2(\mathbf{q},\omega)$ exhibit high intensities at higher frequency domains similar to $\Gamma_{\mathbf{q},\mathrm{LO}}(\omega)$ by the energy conservation $\delta(\omega - \Omega_{\lambda'} - \Omega_{\lambda''})$ in equation (8). This is considered as the main reason why the LO modes show strong anharmonicity. To discuss more details of the LO-mode spectral shapes, $\Phi^{\tilde{\rho}\Phi}_{\lambda\lambda'\lambda''}$ is necessary, since $\Gamma_{\mathbf{q},\mathrm{LO}}(\omega)$ show more q-point dependence than $N_2(\mathbf{q},\omega)$. This is attributed to wave-like property of the three phonon interactions.

4.5. Disconnections of LO-mode branch on Γ–L path

In figures 1 and 2, the LO-mode branches of $A_{\mathbf{q}\nu}(\omega)$ look disconnected on the Γ–L paths, though the disconnection is less clear in NaCl. In each LO-mode branch, a pair of peaks of $A_{\mathbf{q},\mathrm{LO}}(\omega)$ gradually change their intensity ratio as increasing u of $\mathbf{q} = (u,u,u)$ on the Γ–L path. The pair of the peaks of KCl are pointed by small arrows in the panel of $u = 0.123$ in figure 6. The peak at lower frequency side (p1) is a typical main-peak appearing at $\omega_{\mathrm{p1}} \sim \Omega_{\mathbf{q},\mathrm{LO}} + \Delta_{\mathbf{q},\mathrm{LO}}(\omega_{\mathrm{p1}})$. The other peak at higher frequency side (p2) reflects spike-like change of $\Delta_{\mathbf{q},\mathrm{LO}}(\omega)$

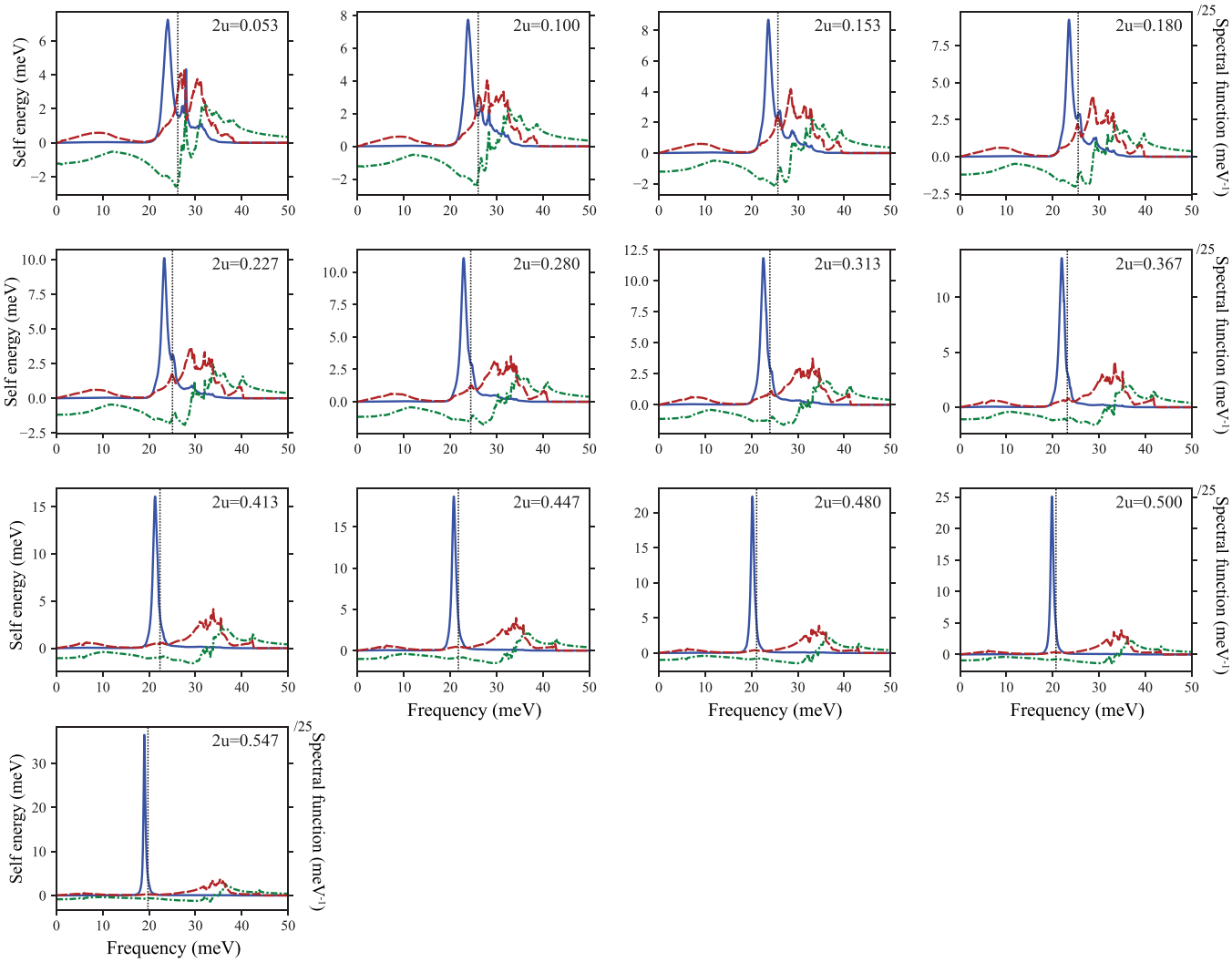

Figure 7. Real and imaginary parts of self-energies and renormalized frequencies of KCl at q-points on the Γ–X path. Each panel corresponds to that in figure 4. The dashed-dotted (green) and dashed (red) curves show the real ($\Delta_{\mathbf{q},\mathrm{LO}}(\omega)$) and imaginary ($\Gamma_{\mathbf{q},\mathrm{LO}}(\omega)$) parts of the self-energies, respectively. The solid (blue) curves show the spectral functions ($A_{\mathbf{q},\mathrm{LO}}(\omega)$), that are the same as those in figure 4. The vertical dotted lines indicate the renormalized frequencies ($\Omega_{\mathbf{q},\mathrm{LO}}$).

near ω_{p2}. The frequency of the peak p2 is higher than $\Omega_{\mathbf{q},\mathrm{LO}} + \Delta_{\mathbf{q},\mathrm{LO}}(\omega_{\mathrm{p2}})$, and the intensity of $A_{\mathbf{q},\mathrm{LO}}(\omega_{\mathrm{p2}})$ comes from the high-frequency-side tail of the bell-shaped function centered at $\Omega_{\mathbf{q},\mathrm{LO}} + \Delta_{\mathbf{q},\mathrm{LO}}(\omega_{\mathrm{p2}})$. $A_{\mathbf{q},\mathrm{LO}}(\omega)$ sharply decays moving away from ω_{p2} since the spike-like $\Delta_{\mathbf{q},\mathrm{LO}}(\omega)$ increases $\omega - [\Omega_{\mathbf{q},\mathrm{LO}} + \Delta_{\mathbf{q},\mathrm{LO}}(\omega)]$ on both sides of the frequency ω_{p2}.

In figure 6, we can see that the position of the spike-like $\Delta_{\mathbf{q},\mathrm{LO}}(\omega)$ shifts to the lower frequency side as increasing u of $\mathbf{q} = (u, u, u)$. This is seen clearly in the left panel of figure 9 as a line of the spike-like $\Delta_{\mathbf{q},\mathrm{LO}}(\omega)$ extending from just above the top of the LO-mode branch (∼25 meV) at the Γ-point. The curve $\Omega_{\mathbf{q},\mathrm{LO}}$ crosses this line around $u = 0.1$. At $u > 0.1$, the peak p2 grows to become another main-peak by increasing u. In this way, the disconnection of the LO-mode branch appears. The line of the spike-like $\Delta_{\mathbf{q},\mathrm{LO}}(\omega)$ is found on the Γ–X path side. However, the disconnection does not appear, since $\Omega_{\mathbf{q},\mathrm{LO}}$ does not cross the line. Compared with KCl, the line of the spike-like $\Delta_{\mathbf{q},\mathrm{LO}}(\omega)$ is less clear for NaCl as shown in figure 10.

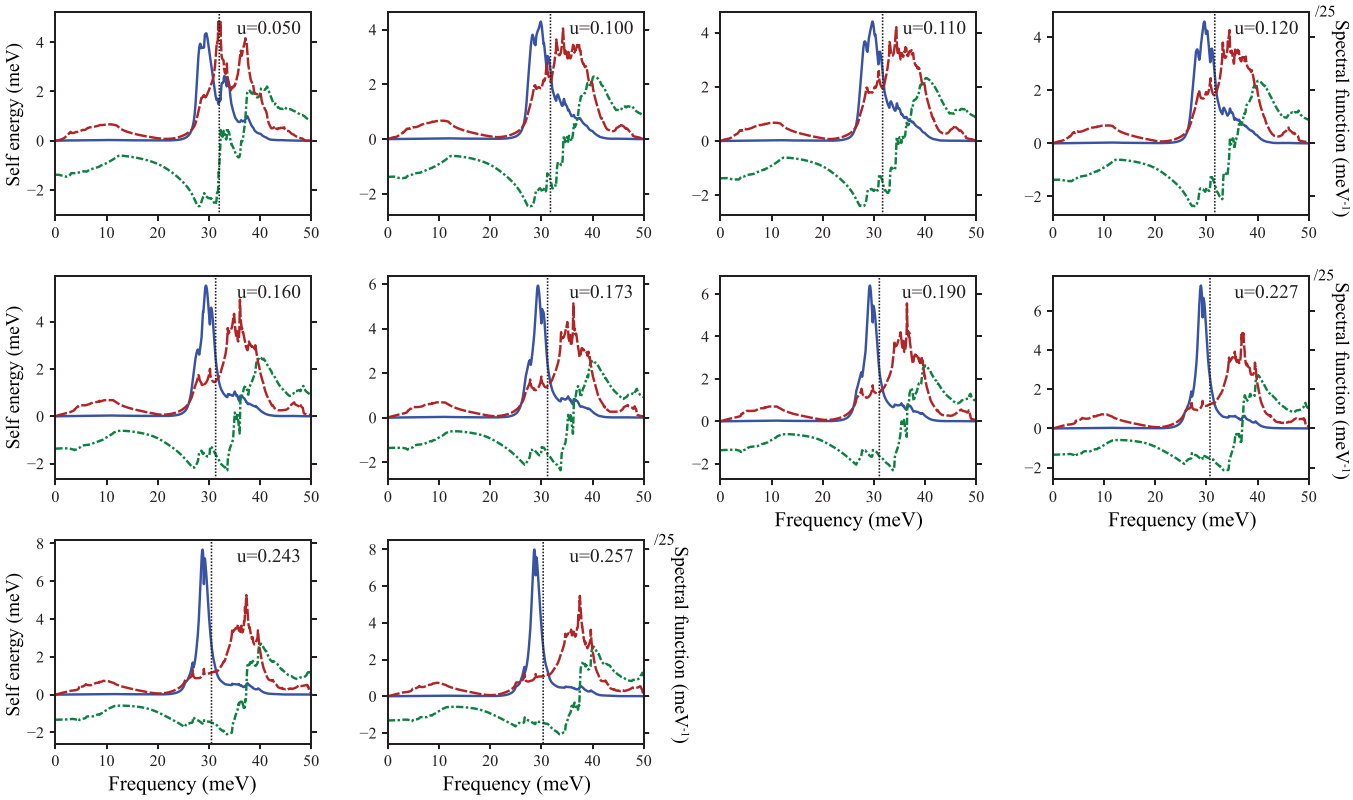

Figure 8. Real and imaginary parts of self-energies and renormalized frequencies of NaCl at q-points on the Γ–L path. Each panel corresponds to that in figure 5. The solid (blue) curves show the spectral functions $(A_{\mathbf{q},\mathrm{LO}}(\omega))$. The dashed-dotted (green) and dashed (red) curves show the real $(\Delta_{\mathbf{q},\mathrm{LO}}(\omega))$ and imaginary $(\Gamma_{\mathbf{q},\mathrm{LO}}(\omega))$ parts of the self-energies, respectively. The solid (blue) curves show the spectral functions, that are the same as those in figure 5. The vertical dotted lines indicate the renormalized frequencies $(\Omega_{\mathbf{q},\mathrm{LO}})$.

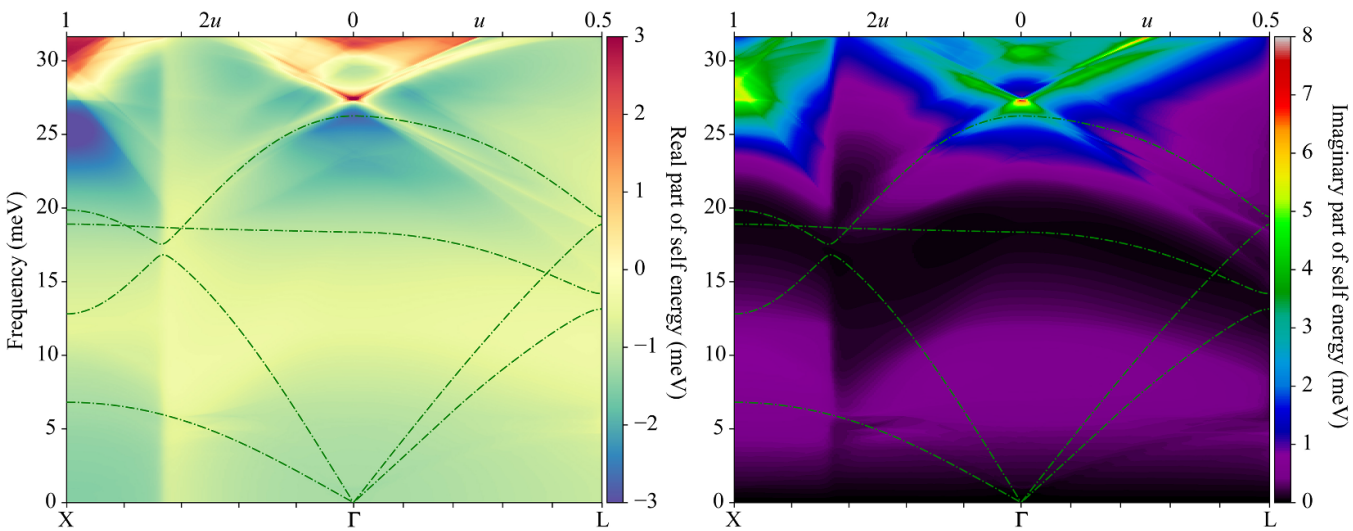

Figure 9. (Left panel) Real $(\Delta_{\mathbf{q},\mathrm{LO}}(\omega))$ and (right panel) imaginary $(\Gamma_{\mathbf{q},\mathrm{LO}}(\omega))$ parts of self-energies obtained for the LO mode of KCl at 300 K. The (green) dashed-dotted curves show the renormalized frequencies, $\Omega_{\mathbf{q}\nu}$.

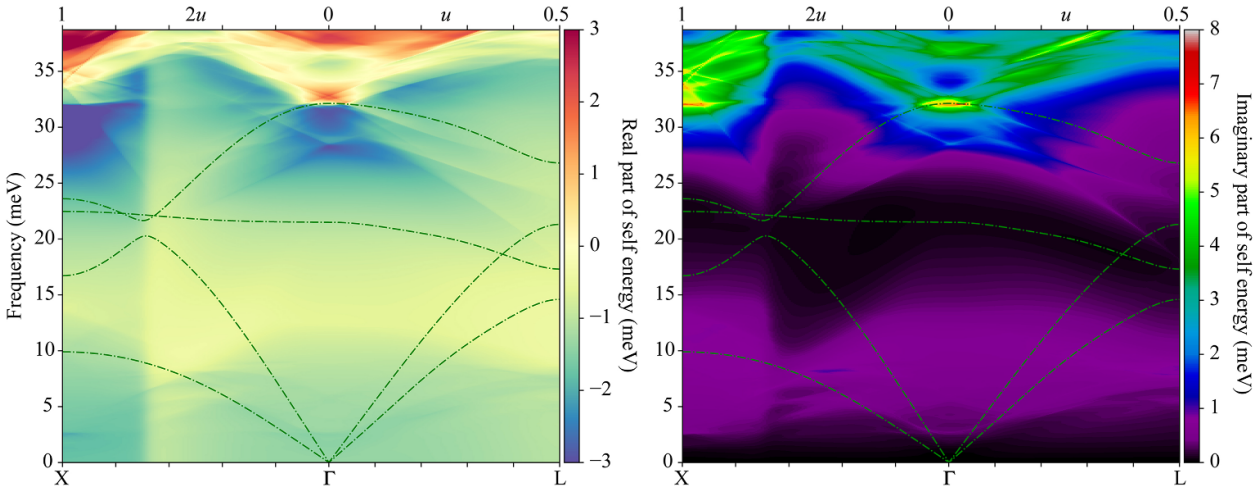

Figure 10. (Left panel) Real $(\Delta_{\mathbf{q},\mathrm{LO}}(\omega))$ and (right panel) imaginary $(\Gamma_{\mathbf{q},\mathrm{LO}}(\omega))$ parts of self-energies obtained for the LO mode of NaCl at 300 K. The (green) dashed-dotted curves show the renormalized frequencies, $\Omega_{\mathbf{q}\nu}$.

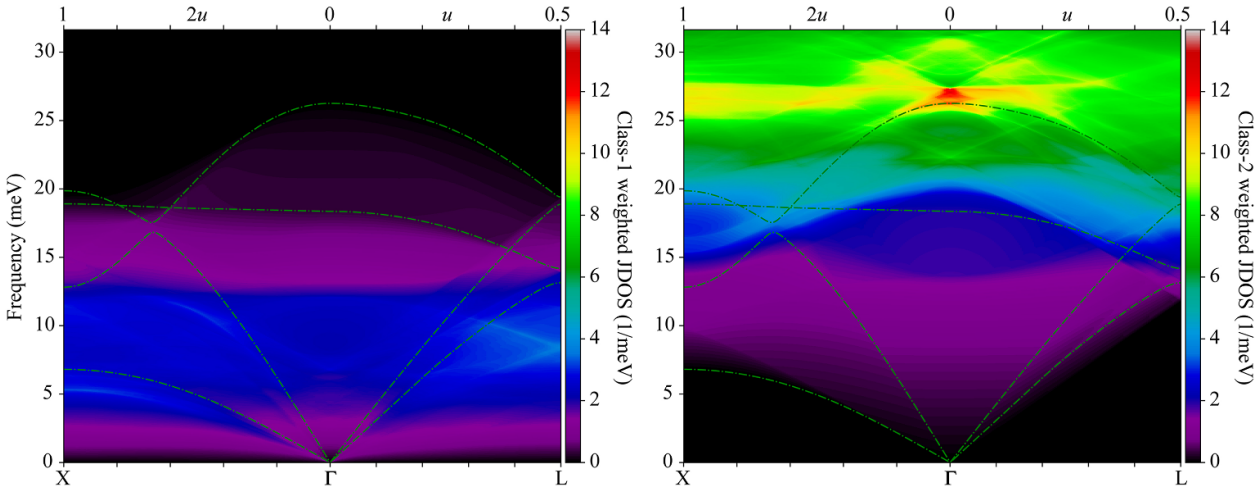

Figure 11. Weighted JDOS of class 1 (left panel, $N_2^{(1)}(\mathbf{q},\omega)$) and class 2 (right panel, $N_2^{(2)}(\mathbf{q},\omega)$) of KCl at 300 K. The (green) dashed-dotted curves show the renormalized frequencies, Ω_λ.

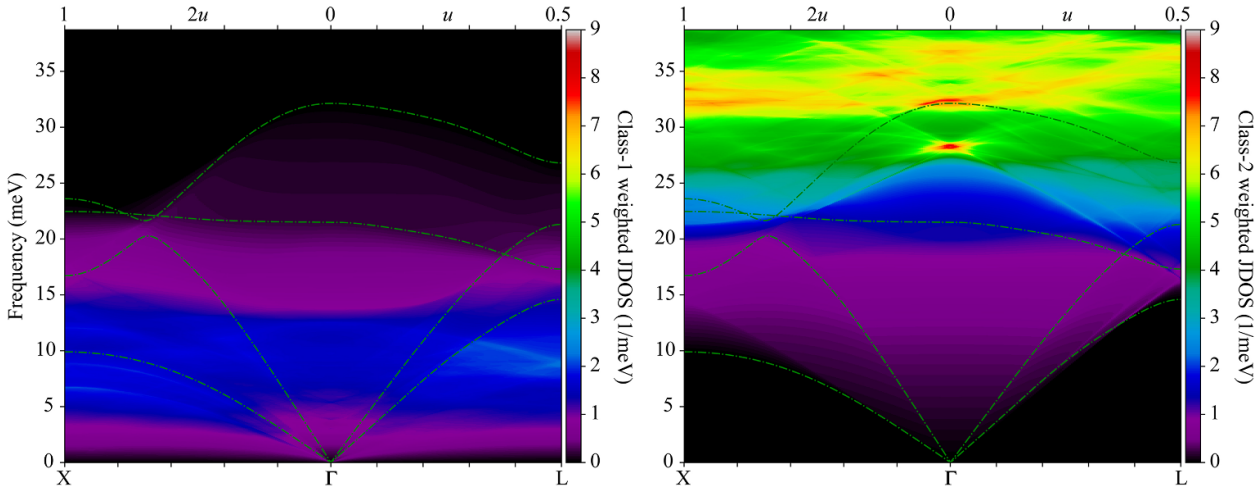

Figure 12. Weighted JDOS of class 1 (left panel, $N_2^{(1)}(\mathbf{q},\omega)$) and class 2 (right panel, $N_2^{(2)}(\mathbf{q},\omega)$) of NaCl at 300 K. The (green) dashed-dotted curves show the renormalized frequencies, Ω_λ.

5. Summary

In this study, we measured the LO-mode phonon branches of KCl and NaCl using IXS at 300 K and calculated their spectral functions using the phonon calculation under the SSCHA method to investigate their strong anharmonicity. The spectral shapes of the IXS measurements and calculations showed good agreements. From the calculated spectral functions, we found the multiple peaks of the LO-mode spectra and the disconnections of the LO-mode branches on the Γ–L paths in KCl and NaCl, which were unclear in the IXS measurements due to the limited energy resolution. From the calculations, we analyzed the spectral shapes of the strongly anharmonic LO-modes and how the disconnections of the LO-mode branches appear using the phonon self-energies and renormalized phonon frequencies.

Data availability statement

All data that support the findings of this study are included within the article (and any supplementary files).

Acknowledgments

This work was supported by MEXT Japan through ESISM (Elements Strategy Initiative for Structural Materials) of Kyoto University and JSPS KAKENHI Grant Numbers JP21K04632 and JP21K03424. The synchrotron experiments were performed at the BL35XU of SPring-8 with the approval of the Japan Synchrotron Radiation Research Institute (JASRI) (Proposal Nos. 2017A1042, 2017B1297 and 2018A1298).

Appendix A. Phonon self energy

In appendices, the phonon modes $(\mathbf{q},\nu)$ and $(-\mathbf{q},\nu)$ are abbreviated by λ and $-\lambda$, respectively. In this appendix, formula of the phonon self-energy used in this study is presented. Three phonon interaction strength $\Phi^{\tilde{\rho}_\Phi}_{\lambda\lambda'\lambda''}$ is given as

$$\begin{aligned}\Phi^{\tilde{\rho}_\Phi}_{\lambda\lambda'\lambda''} = &\frac{1}{\sqrt{N}}\frac{1}{3!}\sum_{\kappa\kappa'\kappa''}\sum_{jj'j''} W_{\lambda,\kappa j}W_{\lambda',\kappa' j'}W_{\lambda'',\kappa'' j''}\\ &\times\sqrt{\frac{\hbar}{2m_\kappa\Omega_\lambda}}\sqrt{\frac{\hbar}{2m_{\kappa'}\Omega_{\lambda'}}}\sqrt{\frac{\hbar}{2m_{\kappa''}\Omega_{\lambda''}}}\\ &\times\sum_{l'l''}\Phi^{\tilde{\rho}_\Phi}_{0\kappa j,l'\kappa' j',l''\kappa'' j''}\\ &\times \mathrm{e}^{i\mathbf{q}'\cdot(\mathbf{r}_{l'\kappa'}-\mathbf{r}_{0\kappa})}\mathrm{e}^{i\mathbf{q}''\cdot(\mathbf{r}_{l''\kappa''}-\mathbf{r}_{0\kappa})}\\ &\times \mathrm{e}^{i(\mathbf{q}+\mathbf{q}'+\mathbf{q}'')\cdot\mathbf{r}_{0\kappa}}\Delta(\mathbf{q}+\mathbf{q}'+\mathbf{q}''),\end{aligned} \tag{A1}$$

where N is the number of primitive cells, and m_κ and $\mathbf{r}_{l\kappa}$ are the atomic mass and position in the primitive cell, respectively. The symbol $\Delta(\mathbf{q}+\mathbf{q}'+\mathbf{q}'')$ means 1 if $\mathbf{q}+\mathbf{q}'+\mathbf{q}''$ is a reciprocal lattice vector, otherwise 0. $W_{\lambda,\kappa j}$ is the phonon eigenvector obtained as the solution of the dynamical matrix of Φ. The phase factor convention of the the phonon eigenvectors is based on the same definition of the dynamical matrix as written in [51].

We write real and imaginary parts of the self-energy as

$$\Sigma_\lambda(\omega) = \Delta_\lambda(\omega) - i\Gamma_\lambda(\omega), \tag{A2}$$

where

$$\begin{aligned}\Delta_\lambda(\omega) = &\frac{18\pi}{\hbar^2}\sum_{\lambda'\lambda''}\left|\Phi^{\tilde{\rho}_\Phi}_{-\lambda\lambda'\lambda''}\right|^2\\ &\times\left\{\left[\frac{(n_{\lambda'}+n_{\lambda''}+1)}{(\omega-\Omega_{\lambda'}-\Omega_{\lambda''})_\mathrm{p}} - \frac{(n_{\lambda'}+n_{\lambda''}+1)}{(\omega+\Omega_{\lambda'}+\Omega_{\lambda''})_\mathrm{p}}\right]\right.\\ &\left.+\left[\frac{(n_{\lambda'}-n_{\lambda''})}{(\omega+\Omega_{\lambda'}-\Omega_{\lambda''})_\mathrm{p}} - \frac{(n_{\lambda'}-n_{\lambda''})}{(\omega-\Omega_{\lambda'}+\Omega_{\lambda''})_\mathrm{p}}\right]\right\},\end{aligned} \tag{A3}$$

and

$$\begin{aligned}\Gamma_\lambda(\omega) = &\frac{18\pi}{\hbar^2}\sum_{\lambda'\lambda''}\left|\Phi^{\tilde{\rho}_\Phi}_{-\lambda\lambda'\lambda''}\right|^2\\ &\times\{(n_{\lambda'}+n_{\lambda''}+1)[\delta(\omega-\Omega_{\lambda'}-\Omega_{\lambda''})\\ &-\delta(\omega+\Omega_{\lambda'}+\Omega_{\lambda''})]+(n_{\lambda'}-n_{\lambda''})\\ &\times[\delta(\omega+\Omega_{\lambda'}-\Omega_{\lambda''})-\delta(\omega-\Omega_{\lambda'}+\Omega_{\lambda''})]\},\end{aligned} \tag{A4}$$

respectively.

Appendix B. Convergence of SSCHA Helmholtz free energy

SSCHA Helmholtz free energy is considered as a good measure of convergence of the force constants. The SSCHA Hermholtz free energy $\mathcal{F}_\Phi$ is written as [12, 34, 36, 40],

$$\mathcal{F}_\Phi = \tilde{F}_\Phi - \langle\tilde{V}_\Phi\rangle_{\tilde{\rho}_\Phi} + \langle V\rangle_{\tilde{\rho}_\Phi}, \tag{B1}$$

where $\tilde{F}_\Phi$ and $\langle\tilde{V}_\Phi\rangle_{\tilde{\rho}_\Phi}$ are the harmonic Helmholtz free energy and potential energy, respectively, and $\langle V\rangle_{\tilde{\rho}_\Phi}$ is the potential energy under $\tilde{\rho}_\Phi$. $\tilde{F}_\Phi$ is given as

$$\tilde{F}_\Phi = \frac{1}{2}\sum_\lambda\hbar\Omega_\lambda + k_\mathrm{B}T\sum_\lambda\ln\left[1-\exp(-\hbar\Omega_\lambda/k_\mathrm{B}T)\right]. \tag{B2}$$

$\langle\tilde{V}_\Phi\rangle_{\tilde{\rho}_\Phi}$ is given by equation (A16) of [36] as

$$\langle\tilde{V}_\Phi\rangle_{\tilde{\rho}_\Phi} = \frac{1}{2}\sum_{l\kappa j,l'\kappa' j'}\Phi_{l\kappa j,l'\kappa' j'}\langle u_{l\kappa j}u_{l'\kappa' j'}\rangle_{\tilde{\rho}_\Phi} \tag{B3}$$

$$\begin{aligned}&= \frac{1}{2}\sum_{l\kappa j,l'\kappa' j'}\frac{\Phi_{l\kappa j,l'\kappa' j'}}{N\sqrt{m_\kappa m_{\kappa'}}}\sum_\lambda\sigma^2_\lambda(T)\\ &\quad\times W^*_{\lambda,\kappa j}W_{\lambda,\kappa' j'}\mathrm{e}^{i\mathbf{q}\cdot(\mathbf{r}_{l'\kappa'}-\mathbf{r}_{l\kappa})},\end{aligned} \tag{B4}$$

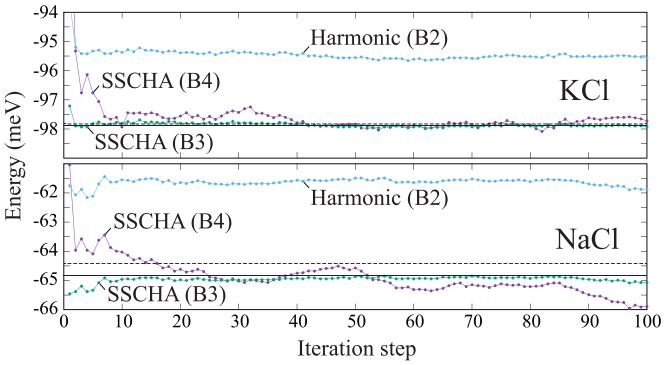

Figure 13. Energy convergences of SSCHA Helmholtz free energies $\mathcal{F}_\Phi$ (equation (B1)) of KCl (top) and NaCl (bottom) per primitive cells with respect to iteration step. In each figure, the dots labeled by SSCHA (B3) and SSCHA (B4) show the $\mathcal{F}_\Phi$ in which $\langle \tilde{V}_\Phi \rangle_{\tilde{\rho}_\Phi}$ are computed following equations (B3) and (B4), respectively, and those labeled by Harmonic (B2) depict the harmonic Helmholtz free energies $\tilde{F}_\Phi$ (equation (B2)). The lines connecting the dots are guides to the eye. The solid and dashed horizontal lines in each figure are the $\mathcal{F}_\Phi$ computed from 4000 supercells generated using Φ obtained at the last iteration step with $\langle \tilde{V}_\Phi \rangle_{\tilde{\rho}_\Phi}$ by equations (B3) and (B4), respectively.

where the second equation is derived from the displacement operator:

$$u_{l\kappa j} = \left(\frac{1}{Nm_\kappa}\right)^{\frac{1}{2}} \sum_\lambda Q_\lambda W_{\lambda,\kappa j} e^{i\mathbf{q}\cdot\mathbf{r}_{l\kappa}}$$
$$= \left(\frac{\hbar}{2Nm_\kappa}\right)^{\frac{1}{2}} \sum_\lambda \Omega_\lambda^{-\frac{1}{2}} (\hat{a}_\lambda + \hat{a}^\dagger_{-\lambda}) W_{\lambda,\kappa j} e^{i\mathbf{q}\cdot\mathbf{r}_{l\kappa}}.$$

Figure 13 shows the calculated values of $\mathcal{F}_\Phi$ of KCl and NaCl at iteration steps using the $2 \times 2 \times 2$ supercells. In equation (B1), $\langle V \rangle_{\tilde{\rho}_\Phi}$ were obtained from electronic total energies of the supercells with generated finite displacements actually used to compute Φ relative to those energies without displacements. $\langle \tilde{V}_\Phi \rangle_{\tilde{\rho}_\Phi}$ were calculated in two ways as given in equations (B3) and (B4). The values of the former were computed from the displacements same as those used for the computation of $\langle V \rangle_{\tilde{\rho}_\Phi}$, and those of the latter were calculated from phonon frequencies and eigenvectors of Φ. We can see $\mathcal{F}_\Phi$ with $\langle \tilde{V}_\Phi \rangle_{\tilde{\rho}_\Phi}$ of equation (B3) is a more stable measure than $\mathcal{F}_\Phi$ with $\langle \tilde{V}_\Phi \rangle_{\tilde{\rho}_\Phi}$ of equation (B4). The difference between them was found to be smaller in KCl than in NaCl. As the references, $\mathcal{F}_\Phi$ were also computed using 4000 supercells generated from Φ obtained at the last iteration step for each of KCl and NaCl. In KCl, those with $\langle \tilde{V}_\Phi \rangle_{\tilde{\rho}_\Phi}$ of equations (B3) and (B4) are equivalent within the energy range of the figure, and in NaCl, they are distinguishable. This may indicate more iteration steps are needed for NaCl than KCl. Another attempt of NaCl calculation with 200 iteration steps was performed and the result is presented in figure 14. Difference between $\mathcal{F}_\Phi$ computed using 4000 supercells from equations (B3) and (B4) is smaller than that in figure 13. This probably indicates the better convergence of the force constants. However this minor difference impacted little on the calculation result of the spectral function shapes.

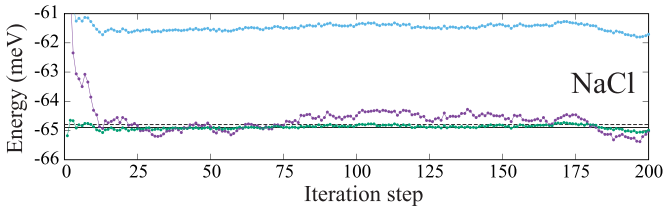

Figure 14. Energy convergences of SSCHA Helmholtz free energies of NaCl. The SSCHA iteration was performed twice longer than that in figure 14. The points and lines show values as explained in figure 13.

ORCID iDs

Atsushi Togo https://orcid.org/0000-0001-8393-9766
Terumasa Tadano https://orcid.org/0000-0002-8132-2161

References

[1] Hohenberg P and Kohn W 1964 *Phys. Rev.* **136** B864
[2] Kohn W and Sham L J 1965 *Phys. Rev.* **140** A1133
[3] Kunc K and Martin R M 1982 *Phys. Rev. Lett.* **48** 406
[4] Giannozzi P, de Gironcoli S, Pavone P and Baroni S 1991 *Phys. Rev.* B **43** 7231
[5] Gonze X, Charlier J-C, Allan D C and Teter M P 1994 *Phys. Rev.* B **50** 13035
[6] Gonze X and Lee C 1997 *Phys. Rev.* B **55** 10355
[7] Parlinski K, Li Z Q and Kawazoe Y 1997 *Phys. Rev. Lett.* **78** 4063
[8] Ziman J M 1960 *Electrons and Phonons: The Theory of Transport Phenomena in Solids* (Oxford: Oxford University Press)
[9] Wallace D C 1998 *Thermodynamics of Crystals* (New York: Dover Publications)
[10] Ashcroft N W and Mermin N D 1976 *Solid State Physics* (Belmont: Thomson Learning)
[11] Gonze X and Vigneron J-P 1989 *Phys. Rev.* B **39** 13120
[12] Errea I, Calandra M and Mauri F 2013 *Phys. Rev. Lett.* **111** 177002
[13] Hellman O, Steneteg P, Abrikosov I A and Simak S I 2013 *Phys. Rev.* B **87** 104111
[14] Tadano T and Tsuneyuki S 2015 *Phys. Rev.* B **92** 054301
[15] Wei B, Sun Q, Li C and Hong J 2021 *Sci. China Phys. Mech. Astron.* **64** 117001
[16] Kulda J, Debernardi A, Cardona M, de Geuser F and Haller E E 2004 *Phys. Rev.* B **69** 045209
[17] Baron A Q R, Uchiyama H, Heid R, Bohnen K P, Tanaka Y, Tsutsui S, Ishikawa D, Lee S and Tajima S 2007 *Phys. Rev.* B **75** 020505
[18] Li C W *et al* 2014 *Phys. Rev. Lett.* **112** 175501
[19] Giura P, Paulatto L, He F, Lobo R P S M, Bosak A, Calandrini E, Paolasini L and Antonangeli D 2019 *Phys. Rev.* B **99** 220304
[20] Ding J *et al* 2020 *Proc. Natl Acad. Sci.* **117** 3930
[21] Lanigan-Atkins T *et al* 2021 *Nat. Mater.* **20** 977
[22] Voneshen D J, Walker H C, Refson K and Goff J P 2017 *Phys. Rev. Lett.* **118** 145901
[23] Squires G L 2012 *Introduction to the Theory of Thermal Neutron Scattering* (Cambridge: Cambridge University Press)
[24] d'Astuto M and Krisch M 2010 *Collect. SFN* **10** 487
[25] Raunio G and Almqvist L 1969 *Phys. Status Solidi* b **33** 209
[26] Raunio G, Almqvist L and Stedman R 1969 *Phys. Rev.* **178** 1496

[27] Schmunk R E and Winder D R 1970 *J. Phys. Chem. Solids* **31** 131
[28] Rohatgi A 2021 Webplotdigitizer: version 4.5 (available at: https://automeris.io/WebPlotDigitizer)
[29] Ravichandran N K and Broido D 2018 *Phys. Rev.* B **98** 085205
[30] Baron A, Tanaka Y, Goto S, Takeshita K, Matsushita T and Ishikawa T 2000 *J. Phys. Chem. Solids* **61** 461
[31] Baron A Q R 2016 High-resolution inelastic x-ray scattering I: context, spectrometers, samples and superconductors *Synchrotron Light Sources and Free-Electron Lasers: Accelerator Physics, Instrumentation and Science Applications* ed E J Jaeschke, S Khan, J R Schneider and J B Hastings (Cham: Springer International Publishing) pp 1643–719
[32] Baron A Q R 2016 High-resolution inelastic x-ray scattering II: scattering theory, harmonic phonons and calculations *Synchrotron Light Sources and Free-Electron Lasers: Accelerator Physics, Instrumentation and Science Applications* ed E J Jaeschke, S Khan, J R Schneider and J B Hastings (Cham: Springer International Publishing) pp 1721–57
[33] Baron A Q R 2015 Introduction to high-resolution inelastic x-ray scattering (arXiv:1504.01098)
[34] Errea I, Calandra M and Mauri F 2014 *Phys. Rev.* B **89** 064302
[35] Paulatto L, Errea I, Calandra M and Mauri F 2015 *Phys. Rev.* B **91** 054304
[36] Bianco R, Errea I, Paulatto L, Calandra M and Mauri F 2017 *Phys. Rev.* B **96** 014111
[37] Bianco R, Errea I, Calandra M and Mauri F 2018 *Phys. Rev.* B **97** 214101
[38] Ribeiro G A S, Paulatto L, Bianco R, Errea I, Mauri F and Calandra M 2018 *Phys. Rev.* B **97** 014306
[39] Aseginolaza U, Bianco R, Monacelli L, Paulatto L, Calandra M, Mauri F, Bergara A and Errea I 2019 *Phys. Rev.* B **100** 214307
[40] Monacelli L, Bianco R, Cherubini M, Calandra M, Errea I and Mauri F 2021 *J. Phys.: Condens. Matter* **33** 363001
[41] Eriksson F, Fransson E and Erhart P 2019 *Adv. Theory Simul.* **2** 1800184
[42] van Roekeghem A, Carrete J and Mingo N 2021 *Comput. Phys. Commun.* **263** 107945
[43] Shulumba N, Hellman O and Minnich A J 2017 *Phys. Rev.* B **95** 014302
[44] Hellman O, Abrikosov I A and Simak S I 2011 *Phys. Rev.* B **84** 180301
[45] Hellman O and Abrikosov I A 2013 *Phys. Rev.* B **88** 144301
[46] Hellman O, Steneteg P, Abrikosov I A and Simak S I 2013 *Phys. Rev.* B **87** 104111
[47] Barragán-Gil L F and Walser R 2018 *Am. J. Phys.* **86** 22
[48] Tadano T and Tsuneyuki S 2018 *J. Phys. Soc. Japan* **87** 041015
[49] Barrett W T and Wallace W E 1954 *J. Am. Chem. Soc.* **76** 366
[50] Togo A and Tanaka I 2015 *Scr. Mater.* **108** 1
[51] Togo A, Chaput L and Tanaka I 2015 *Phys. Rev.* B **91** 094306
[52] Pick R M, Cohen M H and Martin R M 1970 *Phys. Rev.* B **1** 910
[53] Blöchl P E 1994 *Phys. Rev.* B **50** 17953
[54] Kresse G 1995 *J. Non-Cryst. Solids* **193** 222
[55] Kresse G and Furthmüller J 1996 *Comput. Mater. Sci.* **6** 15
[56] Kresse G and Joubert D 1999 *Phys. Rev.* B **59** 1758
[57] Perdew J P, Ruzsinszky A, Csonka G I, Vydrov O A, Scuseria G E, Constantin L A, Zhou X and Burke K 2008 *Phys. Rev. Lett.* **100** 136406
[58] Gajdoš M, Hummer K, Kresse G, Furthmüller J and Bechstedt F 2006 *Phys. Rev.* B **73** 045112
[59] Wu X, Vanderbilt D and Hamann D R 2005 *Phys. Rev.* B **72** 035105
[60] Pizzi G, Cepellotti A, Sabatini R, Marzari N and Kozinsky B 2016 Comput *Mater. Sci.* **111** 218
[61] AiiDA-VASP team (available at: https://github.com/atztogo/aiida-vasp)
[62] AiiDA-phonoxpy team (available at: https://github.com/atztogo/aiida-phonoxpy)
[63] Aroyo M I, Orobengoa D, de la Flor G, Tasci E S, Perez-Mato J M and Wondratschek H 2014 *Acta Crystallogr.* A **70** 126
[64] Mizokami K, Togo A and Tanaka I 2018 *Phys. Rev.* B **97** 224306
[65] Srivastava G P 1990 *The Physics of Phonons* (Boca Raton, FL: CRC Press)